X-ray measurements of laser-solid interactions on the PW laser

P. Koester*, A. Giulietti, D. Giulietti*, L. Labate and L. A. Gizzi
ILIL at IPCF/CNR, also at INFN - section of Pisa, Pisa, Italy

K. L. Lancaster and P. A. Norreys
Central Laser Facility, STFC, Rutherford Appleton Laboratory, HSIC, Didcot, Oxon OX11 0QX, UK

J. S. Green# and R. G. Evans#
Blackett Laboratory, Imperial College, London, UK

Contact | petra.koester@ipcf.cnr.it

S. Baton, F. Perez and M. Koenig
LULI, Ecole Polytechnique, Paris, France

J. Waugh and N. Woolsey
University of York, York, UK

A. Morace and D. Batani
University of Milan-Bicocca, Milan, Italy

K. Akli
Ohio State University, Columbus, USA

* *also at University of Pisa, Italy*

also at Central Laser Facility, STFC, Rutherford Appleton Laboratory, Chilton, Didcot OX11 0QX, UK

Introduction

The generation of fast electrons during the interaction of ultraintense and ultrashort laser pulses with solid materials and the transport of the fast electron beam through matter is currently studied for its importance in a wide range of applications, such as the development of ultrashort X-ray sources [1, 2], proton sources [3] and the Fast Ignition (FI) scheme for Inertial Confinement Fusion [4, 5].

In the FI scheme such an ultra-high current fast electron beam is required to travel through an outer low Z plasma layer in order to deposit its energy in the core of the fusion pellet, creating a hot spot and such igniting the fuel [5]. A detailed knowledge of the physical phenomena underlying the fast electron energy deposition in conditions relevant to FI is therefore of fundamental importance.

The generation of fast electrons and their transport through matter has been studied for many years both experimentally and numerically [6-12]. Previous experiments [13] indicated enhanced stopping of the fast electron beam in plastic materials. The contribution to the enhanced stopping power by physical phenomena dependent on the atomic number Z, such as instabilities [4], could not be excluded in these experiments, as conductive and dielectric target materials with different Z were used.

The joint experiment described here was designed to address fast electron energy deposition phenomena in conditions relevant for the FI scheme. Dielectric low Z (plastic) and mid Z (SiO_2) materials and in metallic (Al) targets were irradiated in the experiment, thus allowing to distinguish between effects arising from the different atomic number Z of the target material and those due to different resistivity of the targets.

Objectives of the experiment and target choice

The idea of the experiment was the investigation of the transport of the energetic electrons generated during the laser-matter interaction in the target material, with particular attention to differences of the electron transport in conducting/dielectric materials with similar atomic number Z and in dielectric target materials with different Z. Therefore, sets of multilayer targets containing a metallic (Al), a dielectric (SiO_2 or plastic) layer respectively, have been used.

The first set of targets consisted of two layers each. The laser-irradiated layer was made of Al, SiO_2 or plastic of two different thicknesses (25 μm or 50 μm), while the second layer, that is the so-called tracer layer, consisted of 1 μm thick Cu. The transverse dimensions of these targets were some mm^2.

The second set of targets, the so-called mass-limited targets, were made of three layers and had transverse dimensions of 400 μm × 400 μm. The laser-irradiated layer was made of Al, SiO_2 or plastic respectively, with thicknesses varying between 1.6 μm and 4 μm. The second layer, made of 1 μm thick Ni, was the tracer layer and the last layer consisted of 1 μm thick plastic material.

Experimental setup

The experiment described here was carried out with the Vulcan Petawatt beam. The laser pulse (λ =1.054 μm) has a pulse duration of 500 fs and an energy per pulse of 700 J. Throughout the experiment a pulse energy of 450 J (measured before the compressor gratings) was used in order to reduce the noise on the diagnostic devices. The laser beam was focused by means of an f/3 off-axis parabolic mirror on the target surface. 50% of the energy was contained in the slightly elliptical focal spot of 6×4 μm^2 size. The average laser intensity in the focal spot was therefore about 5×10^{20} W/cm^2.

A wide range of diagnostic devices has been set up in the experiment. A frequency-doubled part of the laser beam was used as a probe beam for shadowgraphy. The probe beam direction was parallel to the target surface.

The scattered light emitted during the laser-target interaction in the reflection direction of the laser light from the target surface was collected by means of an optical system and was analyzed with a spectrometer. The spectrometer was tuned to detect the emission at 3/2ω and 2ω harmonics of the laser radiation to gain information

about the electron density scalelength and therefore on the plasma formation before the arrival of the main pulse.

Another optical system collected the radiation emitted from the rear surface that is, the side opposite to the laser-irradiated one, of the target foil.

Two X-ray pinhole-cameras equipped with Imaging Plate detectors were mounted on either side of the target surface. An Al foil or a similar material was used to stop visible and infrared radiation. The pinhole diameter was 5 μm and the magnification was 12.3 +/- 0.4 for the front pinhole camera and 11.5 +/- 0.4 for the back pinhole camera.

A spherically bent Quartz crystal was used to perform 2D-imaging with a magnification of about 20 of the Cu Kα emission (for the thick targets containing Cu) and the Ni Lyα emission (for the mass-limited targets containig Ni) respectively. The same spectral range, that is the X-ray radiation around 8 keV was spectrally resolved by the use of a spherically bent Mica crystal in FSSR-1D configuration working in the 11th order of diffraction. Both these diagnostics were equipped with Imaging Plates for the detection of the X-rays. The spectral resolution of the X-ray spectrometer was better than 1/1000.

In some of the experimental shots, in addition to these diagnostics, forward accelerated electrons and protons were detected by means of a custom-made detector called SHEEBA [14]. The detector has been used in direction of the laser beam as well as in the direction normal to the target surface.

Preliminary results from the X-ray measurements

In this section we will describe some preliminary results from the interaction of the laser pulse with the first set of targets, the so-called thick targets. These targets consisted of two layers each. The laser-irradiated layer consisted of Al, SiO_2 or plastic material and was 25 μm or 50 μm thick. The rear side of the targets was coated with a 1 μm thick Cu tracer layer for spectrally resolved X-ray emission measurements.

First we will present some of the results obtained with the front and back pinhole cameras and afterwards we will show results from the Kα measurements.

Figure 1 shows the raw data for the front (the one looking from the laser-irradiated side) and the back pinhole-camera respectively. The images have been obtained from the irradiation of a target with an Al propagation layer of 50 μm thickness. After calculation of the center-of-mass of the X-ray emission region, the average intensity over the circle was calculated for each radial distance from the centre in 10 μm steps. The radial lineouts obtained in this way are displayed together with a gaussian fit in figures 2 and 3 respectively. The front pinhole-camera image shows an X-ray source of about 24 μm FWHM diameter size, whereas the X-ray source seen with the back pinhole-camera has a diameter of about 31 μm FWHM. The peak intensity of the emission is about a factor of 3 less on the back pinhole-camera with respect to the front pinhole-camera.

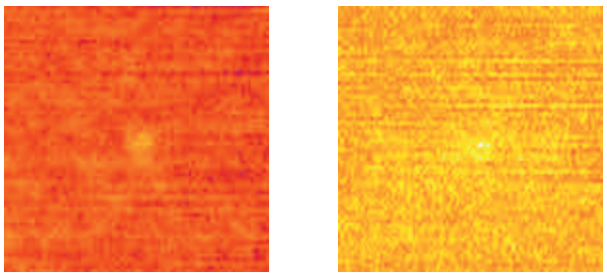

Figure 1. Front (left) and back (right) pinhole camera images obtained from the irradiation of a layered target consisting of a 50 μm thick Al propagation layer with a 1 μm thick Cu coating on the rear surface.

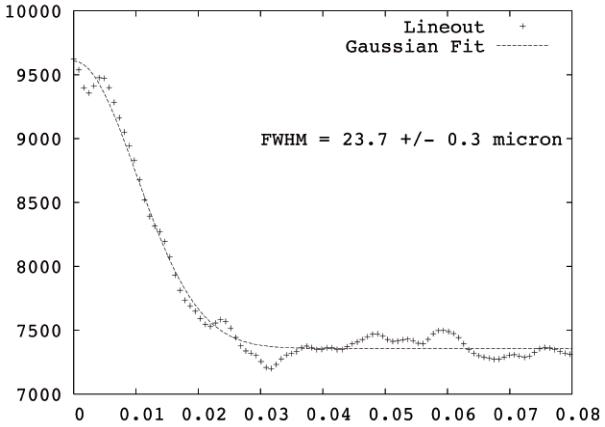

Figure 2. Lineout of Fig.1 (left) and Gaussian Fit. Details see text.

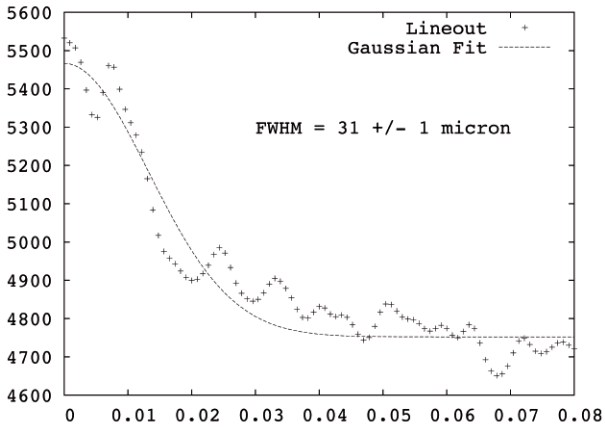

Figure 3. Lineout of Fig.1 (right) and Gaussian Fit. Details see text.

The Kα radiation originating from the Cu tracer layer has been characterized with a 2D imaging crystal. In addition, a bent crystal spectrometer has been used for spectrally resolved measurements of the X-ray emission around the same Kα lines at about 8 keV.

In figure 4 the peak intensities of the monochromatic Cu Kα images obtained with the 2D imaging crystal are shown for targets with an SiO_2 (blue triangles) and an Al (red circles) propagation layer vs. the propagation layer thickness. The FWHM source size was measured to be around 70 μm for all data shots.

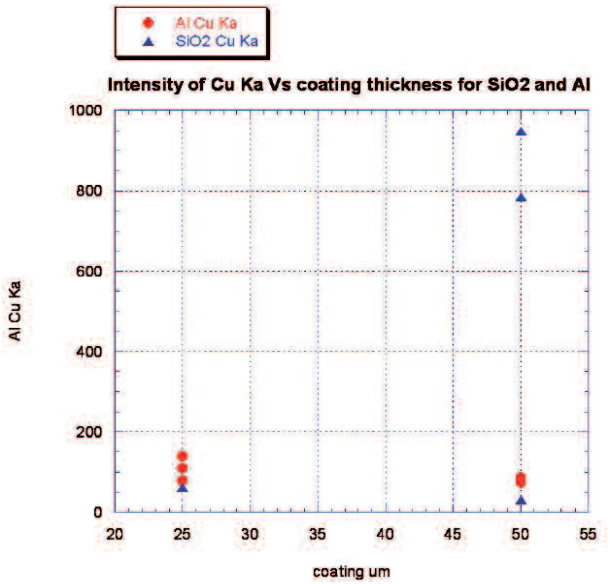

Figure 4. Peak intensity of the Kα emission vs. propagation layer thickness measured with the 2D monochromatic imaging crystal. Data obtained from the irradiation of targets with an Al (red circles) and with an SiO_2 (blue triangles) propagation layer are shown.

The most evident feature in the graph in figure 4 is the bright Kα radiation detected in some of the experimental data points obtained from the interaction of the laser pulse with an SiO_2 front layer. The peak intensity of the Kα line in these data shots is higher by a factor of about 8 with respect to the Kα emission intensity obtained from the targets with an Al front layer.

The X-ray spectra detected with the bent crystal spectrometer show the $K\alpha_1$-line at 1.5406 Å (8.048 keV) and the $K\alpha_2$-line at 1.5444 Å (8.028 keV) originating from the copper back layer. The intensity ratio of the two components is about $I\alpha_2/I\alpha_1=1/2$ as expected[15]. No continuous radiation was observed in the whole spectral range diffracted from the crystal.

Discussion

We will now briefly discuss the pinhole camera images and the Kα measurements.

With respect to the front pinhole camera image, the back pinhole camera image (figure 1) show less intense X-ray emission and a larger emission source size (figures 2 and 3). The X-ray emission observed with the front pinhole camera is mainly due to plasma emission. The X-ray photon energies of the plasma emission are expected to be a few keV, e.g. for a plasma electron temperature of 1.5 keV bremsstrahlung emission peaks around 3 keV[16]. These X-rays will be attenuated to a level below the detection threshold of the back pinhole-camera by the target material itself, as the transmission for radiation up to 4 keV is at most a few percent. Therefore the contribution of the plasma emission to the back pinhole-camera images is negligible.

The radiation detected by the back pinhole camera can be attributed to bremsstrahlung emission from collisions of the fast electrons with the target atoms. Bremsstrahlung from electrons with relativistic energies is emitted in the direction of the fast electron beam in a cone with aperture $1/\gamma$, where γ is the relativistic Lorentz factor of the fast electrons.

The different X-ray source size measured by the front and the back pinhole camera can therefore be explained by the fact, that different physical phenomena are at the origin of the detected X-ray emission.

The Kα measurements presented in the previous section show an enhancement of Kα line intensity by a factor of about 8 in some of the experimental data shots on targets with an SiO_2 propagation layer with respect to the Kα emission intensity obtained from the irradiation of the targets with an Al front layer.

The Kα radiation is generated by inner shell ionization of the target atoms in the Cu tracer layer and successive radiative decay of the atoms in the excited state. The Kα emission intensity is proportional to the number density of fast electrons and to the K shell ionization cross section. The Kα emission detected in the experiment gives therefore information about the fast electron distribution function after the transport of the fast electron beam through the propagation layer.

The fast electron distribution function could not be measured directly in the experiment. The temperature of the initial fast electron population expected from the ponderomotive scaling[17] is around 6.5 MeV for the average laser intensity 5×10^{20} W/cm^2 used in the experiment. Measurements in previous experiments indicate[18] a lower fast electron temperature between 1 and 2 MeV and conversion efficiencies between 40 and 50%.

In figure 5 the K shell ionization cross section is shown as a function of the incoming electron energy. The graph exhibits a maximum around a few tens of keV. For higher energies the cross section decreases, having a minimum at around 1 MeV. For even higher, relativistic energies the K shell ionization cross section increases again. From the graph in figure 5 it is evident that a different fast electron temperature after propagation in the SiO_2 layer and in the Al layer respectively can at most result in an increase of the Kα emission intensity by a factor of about 3. Therefore, propagation effects, such as enhanced stopping of the fast electron beam in dielectric targets cannot completely explain the observed differences.

On the other hand, the interaction conditions at the arrival of the main laser pulse for the SiO_2 target might differ significantly from those for the Al target due to different preplasma formation. SiO_2 has a high ionization threshold (around 10^{12} W/cm^2, whereas in metallic materials such as Al, free electrons are always present and no ionization threshold exists. Preplasma formation is therefore more important in Al than in SiO_2 and the plasma expansion before the arrival of the main laser pulse leads to less steep density gradients for metallic targets.

Clearly, the plasma density profile at the arrival of the main laser pulse affects the fast electron generation. In steeper density profiles the skin depth is reduced leading to less penetration of the electromagnetic fields and thus to less energetic fast electrons[21]. On the other hand,

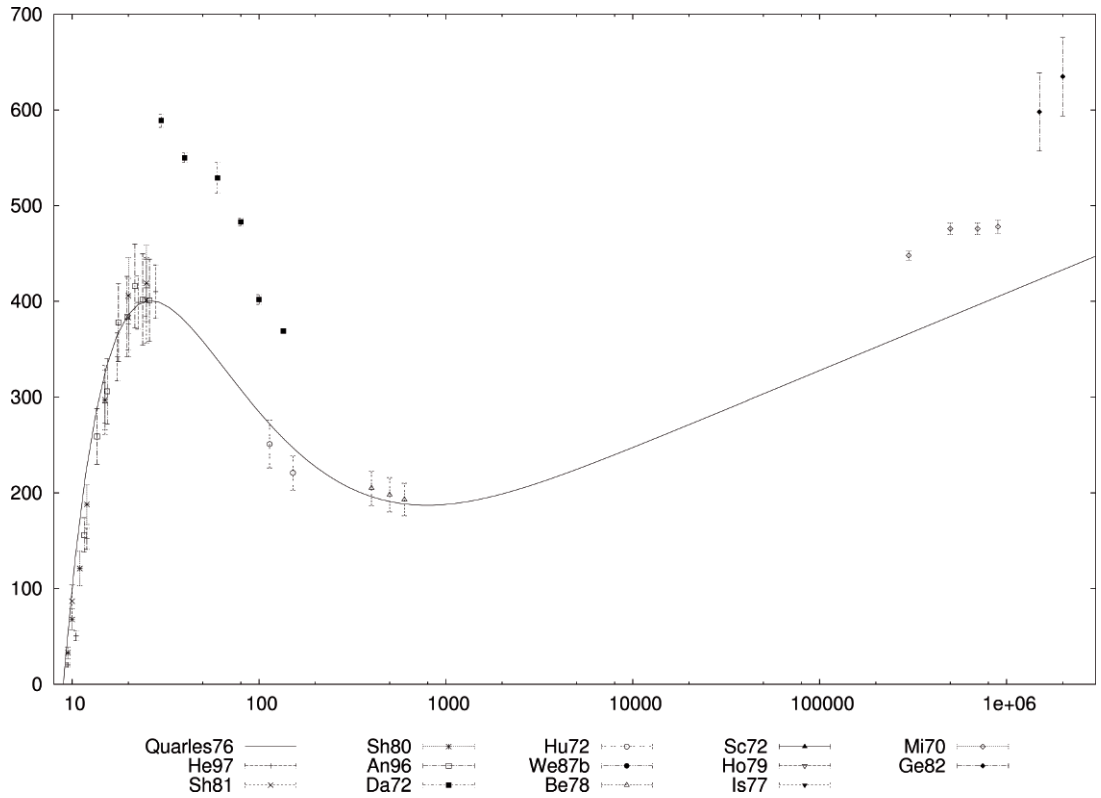

Figure 5. K shell ionization cross section in barn for copper as a function of the incoming electron energy in keV. The experimental data points have been taken from [19] maintaining the same labelling for references therein. The theoretical curve has been plotted according to the formula given by Quarles [20].

conversion efficiencies might not be effected by the density profile, thus leading to a higher number of fast electrons in the case of a steeper density profile. This would result in a higher Kα emission yield.

Conclusions

We reported on X-ray measurements for the study of fast electron energy transport in laser-solid interactions on the Vulcan Petawatt beam.

The back pinhole camera images show a larger X-ray source size with respect to the front pinhole camera images. This difference is attributed to the different physical phenomena at the origin of the X-ray emission detected by the two pinhole cameras.

Enhanced Kα emission generated by the passage of fast electrons in the tracer layer after propagation in an SiO_2 layer was observed. The possible origin of the experimental measurements was preliminarly discussed, taking into account some physical mechanisms occurring during the fast electron transport and the effect of different preplasma formation on the two target types.

Acknowledgements

This work is part of the experimental validation programme of the European HiPER project in Inertial Fusion Energy. One of the authors (P.K.) acknowledges the COST P14 Action for financial support (STSM) for the participation at the experimental campaign at the Vulcan laser facility.

References

1. A. Rousse *et al.*, *Rev. Mod. Phys*. **73**, 17 (2001).
2. C. Reich *et al.*, *Phys. Rev. E* **68**, 056408 (2003).
3. A. J. MacKinnon *et al.*, *Phys. Rev. Lett.* **86**, 1769 (2001).
4. R. G. Evans, *Plasma Phys. Cont. Fusion* **49**, B87 (2007).
5. M. H. Key, *Phys. Plasmas* **14**, 055502 (2007).
6. B. Luther-Davies *et al.*, *Phys. Rev. A* **35**, 4306 (1987).
7. A. R. Bell *et al.*, *Plasma Phys. Controll. Fusion* **39**, 65 (1997).
8. K. B. Wharton *et al.*, *Phys. Rev. Lett.* **81**, 822 (1998).
9. F. Pisani *et al.*, *Phys. Rev. E* **62**, R5927 (2000).
10. D. Batani, *Laser Part. Beams* **20**, 321 (2002).
11. R. J. Mason *et al.*, *Phys. Rev. E* **72**, 015401(R) (2005).
12. P. A. Norreys *et al.*, *Plasma Phys. Controll. Fusion* **48**, L11 (2006).
13. M. Manclossi *et al.*, *Phys. Rev. Lett.* **96**, 125002 (2006).
14. M. Galimberti *et al.*, *Rev. Sci. Instrum.* **76**, 083101 (2005).
15. J. H. Scofield, *Phys. Rev. A* **9**, 1041 (1974).
16. D. Giulietti and L. A. Gizzi, *Il Nuovo Cimento* **21**, 1 (1998).
17. S. C. Wilks *et al.*, *Phys. Rev. Lett.* **69**, 1383 (1992).
18. K. Yasuike *et al.*, *Rev. Sci. Instrum.* **72**, 1236 (2001).
19. M. Liu *et al.*, *Atomic and Nuclear Data Tables* **76**, 213 (2000).
20. C. A. Quarles, *Phys. Rev. A* **13**, 1278 (1975).
21. J. Denavit, *Phys. Rev. Lett.* **69**, 3052 (1992).